

ARTICLE OPEN



Degradation analysis of tribologically loaded carbon nanotubes and carbon onions

T. MacLucas¹✉, P. Grützmacher¹ , S. Husmann^{3,4}, J. Schmauch⁵, S. Keskin³, S. Suarez¹ , V. Presser^{3,4,6}, C. Gachot²✉ and F. Mücklich¹

Coating laser-patterned stainless-steel surfaces with carbon nanotubes (CNT) or carbon onions (CO) forms a tribological system that provides effective solid lubrication. Lubricant retention represents the fundamental mechanism of this system, as storing the particles inside the pattern prevents lubricant depletion in the contact area. In previous works, we used direct laser interference patterning to create line patterns with three different structural depths on AISI 304 stainless-steel platelets. Electrophoretic deposition subsequently coated the patterned surfaces with either CNTs or COs. Ball-on-disc friction tests were conducted to study the effect of structural depth on the solid lubricity of as-described surfaces. The results demonstrated that the shallower the textures, the lower the coefficient of friction, regardless of the applied particle type. This follow-up study examines the carbon nanoparticles' structural degradation after friction testing on substrates patterned with different structural depths (0.24, 0.36, and 0.77 μm). Raman characterization shows severe degradation of both particle types and is used to classify their degradation state within Ferrari's three-stage amorphization model. It was further shown that improving CNT lubricity translates into increasing particle defectivity. This is confirmed by electron microscopy, which shows decreasing crystalline domains. Compared to CNTs, CO-derived tribofilms show even more substantial structural degradation.

npj Materials Degradation (2023)7:31 | <https://doi.org/10.1038/s41529-023-00346-5>

INTRODUCTION

Global efforts to move away from fossil resources kindle the need for oil-free forms of lubrication. Solid lubricants represent an exciting alternative as they offer higher thermal stability, functionality under vacuum, applicability under higher loads, and avoid issues related to containment. A material group that is particularly interesting in this regard and has attracted significant interest from the tribology community are carbon nanoparticles, more specifically, multiwalled carbon nanotubes (CNT) and carbon onions (CO). Due to their respectively cylindrical and spherical shape, it is assumed that these particles can roll when subjected to shear, thus acting like a microscale roller bearing, but in effect, the lubrication mechanism remains speculative. The lubricity of these particles, however, is well documented in the literature regardless of their use as a coating^{1–9}, additive^{10–13}, or composite phase^{14–21}. To better understand their respective lubrication mechanisms, the CNTs' and COs' structural degradation during tribological loading requires more in-depth research.

The standard technique for assessing the structural condition of crystalline and amorphous carbon is Raman spectroscopy. The interpretation of experimental Raman spectra of CNTs and COs is derived primarily from studies on graphite, graphene, and single-walled carbon nanotubes^{22–30}. Morphological differences between these particles (curvature, multilayered structure) affect the polarizability of the carbon bonds and can alter the resulting spectra²⁸. Reinert et al. examined the structural deterioration of CNTs in CNT/nickel composites²¹. Conformal contact friction tests were conducted on a ring-on-block tribometer against an SAE 1045 steel ring at a load of 20 N. As contact pressure increased, more particle defects were observed, and presented a four-stage

model describing the degradation from highly crystalline to nanocrystalline carbon.

In a previous study, we performed friction tests with CNT and CO coatings on laser-patterned stainless-steel surfaces⁹. Direct laser interference patterning (DLIP) was used to create superficial line patterns with a periodicity of 3.5 μm . During DLIP, two or more high-power laser pulses are brought to interfere directly on the substrate surface to create well-defined patterns³¹. The resulting substrate surfaces were then coated by electrophoretic deposition (EPD), a coating technique during which a voltage is applied to conductive substrates immersed in a suspension, causing the dispersed carbon nanoparticles to migrate to the electrode of opposite charge. In the following, the findings of that work are briefly summarized for better understanding. As illustrated in Fig. 1, linear reciprocal ball-on-disc testing was conducted on line-patterned (periodicity = 3.5 μm) stainless-steel substrates with three different structural depths (high-, intermediate-, and low depth, HD, ID, and LD, respectively). The lubricity of the CNT-coated and CO-coated samples was compared to uncoated equivalents at a load of 100 mN. A correlation was identified between lubricity and structural depth, which varied between 0.78 μm (HD), 0.37 μm (ID), and 0.22 μm (LD). The results show that CNT and CO coatings lubricate more efficiently as the structural depth decreases. Patterned but uncoated samples (HD, ID, and LD) exhibit slightly lower COFs than the nonpatterned and uncoated reference⁹. Coating the pattern reduced the COF values considerably over the entire testing period, regardless of particle type. The key finding, however, was the emergence of a trend displayed by the COF development of both CNT- and CO-coated substrates: the lower the structural depth of the pattern, the lower its COF. Although deeper structures retain lubricant particles

¹Chair of Functional Materials, Saarland University, Campus D3.3, Saarbrücken 66123, Germany. ²Institute for Engineering Design and Product Development, TU Wien, Lehnbrunnengasse 6, 1060 Vienna, Austria. ³INM – Leibniz Institute for New Materials, 66123 Saarbrücken, Germany. ⁴Department of Materials Science & Engineering, Saarland University, Campus D2.2, 66123 Saarbrücken, Germany. ⁵Department of Experimental Physics, Campus D2.2, Saarland University, 66123 Saarbrücken, Germany. ⁶saarene – Saarland Center for Energy Materials and Sustainability, Campus C4.2, 66123 Saarbrücken, Germany. ✉email: timothy.maclucas@uni-saarland.de; Carsten.gachot@tuwien.at

better, their lubricity is less effective since the direct particle supply to the contact is hampered by higher slope angles.

This study represents a follow-up to our previous work, and we investigate the degradation process of the CNTs and COs as an integral part of the resulting tribofilms during friction testing. For that purpose, Raman spectroscopy and electron microscopy were used to analyze the nanocarbons' structural condition.

RESULTS AND DISCUSSION

Raman analysis

In the pristine material, the characteristic Raman features of CNTs include the D-, G-, D'-, and G'-band (Fig. 2)^{22,23}. At a laser wavelength of 532 nm, the D-band is located at 1350 cm^{-1} and corresponds to the breathing mode of A_{1g} symmetry. In perfect (highly oriented pyrolytic) graphite (HOPG), this mode is forbidden³² and becomes active in the presence of defects such as grain boundaries or vacancies, among others^{23,29,33}. The (G+D')-band is a convolution of the G- and D'-bands and is among the most pronounced bands in the Raman spectra of CNTs and/or COs. The G-band appears at 1582 cm^{-1} and is associated with the E_{2g} phonon. In pristine CNTs, the (G+D')-band exhibits a distinct shoulder toward higher wavenumbers. This can be attributed to defect-induced double resonance, which gives rise to the D'-band between 1617 cm^{-1} and 1625 cm^{-1} . Like the D-band, the D'-band is activated by crystalline defects²⁴. The dispersive G'-band (or 2D-band) is located around 2700 cm^{-1} at an excitation wavelength of 532 nm and originates from electron-hole intervalley scattering³⁴. It represents an overtone of the D-band and indicates long-range order; hence, it disappears with increasing degradation and/or amorphization^{30,35}.

Quantifying intensity, position, and full width at half maximum (FWHM) of the Raman bands require suitable fittings. The G-band originates from first-order scattering and is, thus, related to one oscillator only (one phonon process)³⁴. Therefore, the G-band is best approximated by a Lorentzian, which is used to describe phonon behavior within the Lorentz oscillator model and thus provides a precise physical meaning. In the case of the D-, D'- and G'-band, which descend from double-resonance Raman scattering corresponding to a convolution of a large number of oscillators (Lorentzian), a single Voigtian is used for approximation. Voigtian peaks are not the preferred choice as they lack the physical background; however, they are suitable for describing a convolution of Lorentzian peaks and providing a proper fitting.

Figure 3a–d depicts the Raman spectra of pristine CNTs and CNTs after tribological testing on the laser-patterned surfaces. Based on the spectral features described previously, a set of indicators can be derived, described in more detail in the following section. In conjunction with the three-stage amorphization model of graphite by Ferrari and Robertson²³, these indicators allow for evaluating the particles' degradation state. We use this framework to assess the defectivity of the CNTs in their respective wear track. The data used for this analysis are listed in Table 1.

The D/G-band ratio (also referred to as the defect index) indicates a measure of crystalline disorder²⁹. Previous studies considered the normalized intensity ratio (I_D/I_G) or the integrated area ratio (A_D/A_G). As certain defects do not affect intensity but lead to a broadening of the band and vice versa²³, we consider both. Figure 3e shows their development as a function of structural depth. Our pristine CNTs exhibit low defectivity with values of 0.57 (I_D/I_G) and 0.70 (A_D/A_G). After friction testing on the coated HD surface, the D-band has grown significantly in intensity; hence the defect index has increased to 1.35 (I_D/I_G) and 1.68 (A_D/A_G). This can be attributed to different degradation processes, such as decreasing crystallite size, breaking covalent bonds, and deformation resulting from the mechanical stress occurring in the contact^{23,27,29}. The defect indices continue to

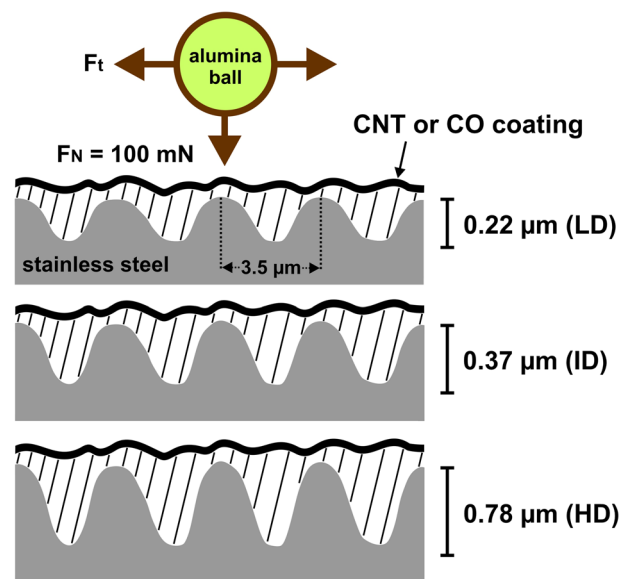


Fig. 1 Cross-section scheme of line-patterned steel substrates with varying structural depths. It illustrates the friction testing conducted on these surfaces coated with either CNTs or COs as conducted by MacLucas et al.⁹

increase for the worn CNTs on ID with an I_D/I_G of 1.39 and an A_D/A_G of 1.83 before reaching a maximum on LD with 1.41 (I_D/I_G) and 2.01 (A_D/A_G). These values agree with those obtained by Cançado et al. for defective graphene²⁴.

A similar development can be observed for the single fit position of the G-band (X_G), which shifts upward as a function of increasing graphitic disorder (Fig. 3e). However, this is less of a shift but more accurately a modification of the band shape owing to the growing D'-band^{21,23}. As a result of the frictional stress the particles are exposed to, X_G shifts from 1582.2 cm^{-1} (pristine) to 1587.1 cm^{-1} (HD), 1589.6 cm^{-1} (ID), and 1589.0 cm^{-1} (LD).

Simultaneously, the development of the purity ratio I_G/I_D (also normalized as proposed by DiLeo et al.³⁶), and its areal equivalent A_G/A_D , show an equally clear (decreasing) trend (Fig. 2f), indicating a strong correlation. This can be explained by incorporating non-carbon impurities, for example, oxygen, into the particles' crystalline structure as they become increasingly defective. While pristine CNTs maintain high purity (1.30 I_G/I_D and 1.73 A_G/A_D), it drops steeply following exposure to tribological load. On HD, the particles show a purity of 0.27 (I_G/I_D) and 0.33 (A_G/A_D), which reduces continuously as structural depth decreases, reaching a minimum of 0.16 (I_G/I_D), respectively, 0.18 (A_G/A_D) on LD. Moreover, Ferreira et al. have shown A_G/A_G to be a reliable indicator in graphene and HOPG as it decreases considerably with increasing defectivity³⁰. Pristine CNT exhibits an A_G/A_G of 1.20 compared to 0.56 on HD after being subjected to tribological load. This is followed by a gradual decrease to a value of 0.42 on ID and, finally, the minimum value of 0.36 on LD (Fig. 3f).

Generally, the FWHM of the G-band (W_G) is used to measure crystallinity or structural disorder. However, Ferreira and co-workers have shown that band broadening due to increasing defectivity is not limited to the G-band. Accordingly, W_D and W_G are included in this analysis³⁰. The FWHM of W_D and W_G show an identical development: the respective FWHM values continuously increase from pristine to HD and ID and then show a jump to a maximum on LD (Fig. 3g). In contrast, W_G remains at roughly the same level except for LD, where a substantial increase occurs. A previously observed pattern repeats itself: exposure to friction

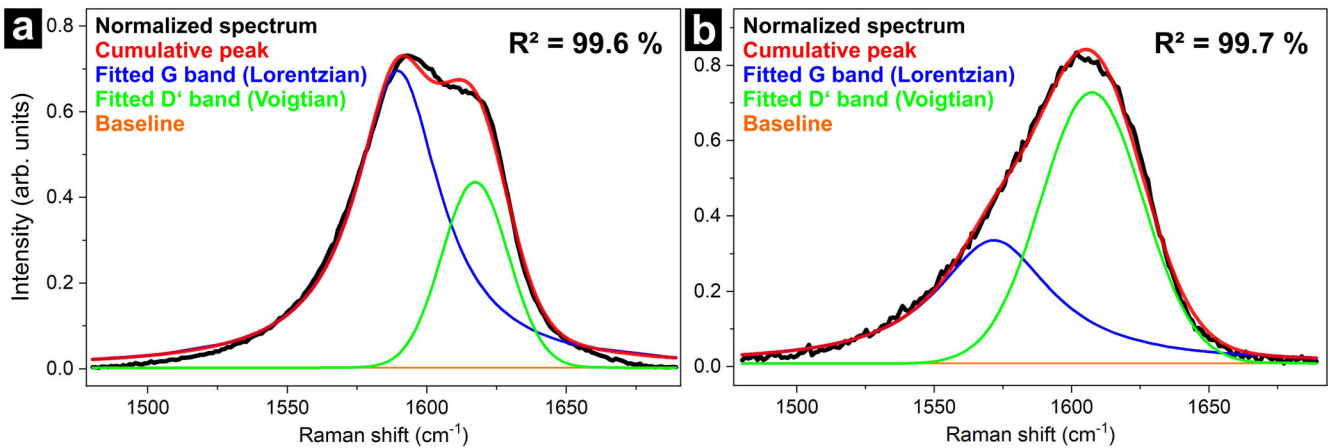


Fig. 2 Two-peak fit of the (G+D')-Raman band. Exemplary two-peak fits of the (G+D')-band in the Raman spectrum of **a** CNTs and **b** COs. A Lorentzian peak shape is used to fit the G-band, and a Voigtian peak profile is used to fit the D'-band.

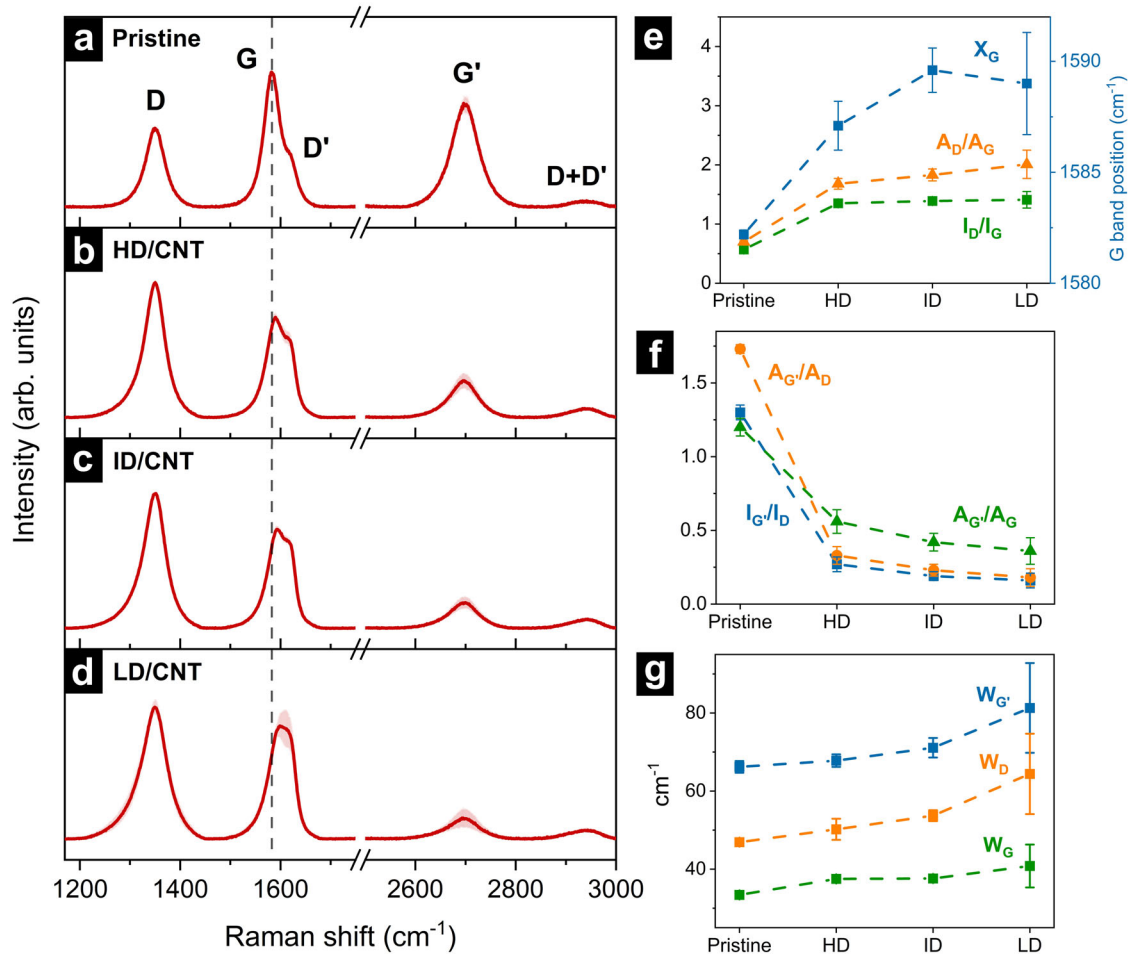


Fig. 3 Raman spectra and indicator developments of CNTs in pristine condition and after tribological testing. Raman spectra of **a** pristine CNTs and CNTs after tribological testing on **b** HD, **c** ID, and **d** LD surfaces, including standard deviation of spectral intensities (red area). Development of **e** I_D/I_G , A_D/A_G , X_G , **f** I_G/I_D , A_G/A_D , A_G/A_G and **g** W_D , W_G , $W_{G'}$ with increasing structural depth (error bars represent standard deviation from three independent measurements).

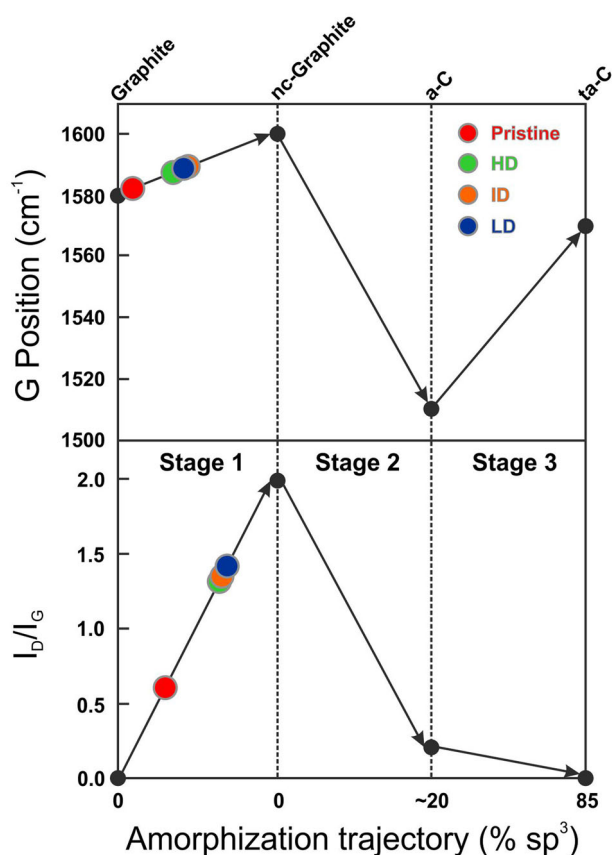
causes the FWHM values and the CNT's defectivity to rise. This disorder further increases as a function of surface pattern depth.

Within Ferrari and Robertson's three-stage amorphization model, CNTs are classified as stage 1 due to the upshift of the

G-band position X_G from 1582.2 cm^{-1} (pristine) to 1589.0 cm^{-1} (LD), indicating a transformation from graphitic to nanocrystalline graphitic carbon (Fig. 4). This is corroborated by the I_D/I_G development with values rising continuously from 0.57 (pristine)

Table 1. Overview of the Raman indicators derived from the spectral features of the respective particles.

	I_D/I_G (-)	A_D/A_G	I_G/I_D	A_G/A_D	A_G/A_G	W_D (cm^{-1})	W_G	W_G	X_G
CNT									
Pristine	0.57 ± 0.01	0.70 ± 0.02	1.30 ± 0.05	1.73 ± 0.03	1.20 ± 0.06	46.9 ± 0.4	33.4 ± 0.2	66.2 ± 1.5	1582.2 ± 0.2
HD	1.35 ± 0.05	1.68 ± 0.09	0.27 ± 0.05	0.33 ± 0.06	0.56 ± 0.08	50.2 ± 2.7	37.5 ± 0.8	67.8 ± 1.6	1587.1 ± 1.1
ID	1.39 ± 0.03	1.83 ± 0.10	0.19 ± 0.03	0.23 ± 0.04	0.42 ± 0.06	53.7 ± 1.4	37.6 ± 1.0	71.1 ± 2.5	1589.6 ± 1.0
LD	1.41 ± 0.14	2.01 ± 0.24	0.16 ± 0.05	0.18 ± 0.06	0.36 ± 0.09	64.4 ± 10.3	40.8 ± 5.5	81.3 ± 11.5	1589.0 ± 2.3
CO									
Pristine	1.50 ± 0.27	1.87 ± 0.26	0.57 ± 0.03	0.65 ± 0.04	1.21 ± 0.16	57.0 ± 1.3	41.7 ± 2.5	69.7 ± 1.4	1576.7 ± 0.8
HD	3.83 ± 1.22	4.80 ± 1.38	0.11 ± 0.03	0.17 ± 0.05	0.76 ± 0.23	78.0 ± 5.1	56.2 ± 4.7	124.6 ± 44.1	1569.0 ± 8.9
ID	2.06 ± 0.62	2.91 ± 0.76	0.15 ± 0.12	0.22 ± 0.14	0.58 ± 0.22	87.1 ± 12.4	54.2 ± 5.4	228.3 ± 176.2	1577.0 ± 7.6
LD	2.69 ± 1.30	3.56 ± 1.50	0.09 ± 0.04	0.15 ± 0.10	0.47 ± 0.20	83.2 ± 10.2	55.2 ± 11.4	172.4 ± 134.7	1577.8 ± 11.9

**Fig. 4** Carbon amorphization trajectory according to Ferrari and Robertson, including data of the characterized CNTs (adapted from ref. 23). It shows a schematic variation of the G-band position and I_D/I_G (obtained with 514 nm) depending on crystallinity as well as sp^2/sp^3 content of the particles.

to 1.41 (LD). However, the condition of the particles on the different surfaces shows finer nuances:

- For HD, although the G- and D'-bands overlap to a large degree, the D'-band shoulder is visible (Fig. 3b) and significantly higher compared to that of the pristine material. As the (D+D')-band is present, the CNTs on this surface are classified as stage 1 (d), which describes an advanced stage of the transformation from mono- to polycrystalline graphite.
- The Raman spectrum of ID closely resembles HD, except that the D'-band shoulder has moved up slightly. Despite all

indicators showing higher defectivity, lower purity, and a stronger upshift of X_G , the CNTs on ID are still classified as stage 1 (d). However, particles on this surface have progressed further on their trajectory toward nanocrystalline graphite compared to those on HD.

- For LD, the distinct shoulder has entirely vanished due to the strong growth of the D'-band. Regarding its shape, the convoluted (G+D')-band can now be considered uniform, which classifies the degradation state of the CNT on LD as stage 1 (e)²⁸. In addition, eight out of nine indicators show the CNTs on LD to be the most defective, with X_G very close to that of the CNTs on ID.

The Raman spectrum of the carbon onions shows the same characteristic bands as the CNTs (Fig. 5a–d). However, the bands' positions may vary slightly due to the more substantial curvature impacting bond polarizability and, thus, the Raman scattering process. The G-band, for example, is shifted slightly downward (1580 cm^{-1}) compared to CNT/graphite (1582 cm^{-1}). In contrast to the CNTs, tribo-induced oxidation does occur during friction testing on CO-coated surfaces, giving rise to an additional broad band around 670 cm^{-1} , a convolution of vibrational modes associated with FeO, Fe_2O_3 , and Fe_3O_4 ³⁷. This can be explained by the fact that, unlike COs, CNTs can form coherent patches on top of the patterns, which effectively separate the sliding surfaces and, thus, prevent oxidation³⁸.

Except for X_G , all indicators show pristine COs to be of superior structural quality and purity than any of the loaded particles (Fig. 5e–g). Further, six out of nine indicators show HD to be more defective than ID. More specifically, the defect and the purity ratios, A_G/A_G and W_G , attribute a higher defectivity to the particles on HD, whereas X_G , W_D , and W_G are higher for those on ID. However, due to their often large standard deviations and associated overlapping, it is difficult to consider the particles of one surface more defective than the other. Four out of nine indicators attribute the highest defectivity to the COs on LD. Concerning the remaining indicators of I_D/I_G , A_D/A_G , W_D , W_G , and W_G , the COs on LD exhibit the second-highest defectivity. Therefore, the entirety of indicators suggests the COs on LD be the most defective overall.

In contrast to the CNTs, the COs indicator values for I_D/I_G and X_G do not fit the three-stage amorphization model after Ferrari and Robertson, which could be attributed to more substantial curvature. However, according to the model, the single peak shape of the G+D'-band observable on all surfaces suggests the particles have surpassed stage 1 (e) and reached stage 2. Thus, the transformation to nanocrystalline graphite is completed. The COs on LD seem to have progressed furthest toward stage 2 (a), representing the initial amorphization phase. Compared to the (G+D')-band of the CNTs on LD, the CO-bands are notably sharper,

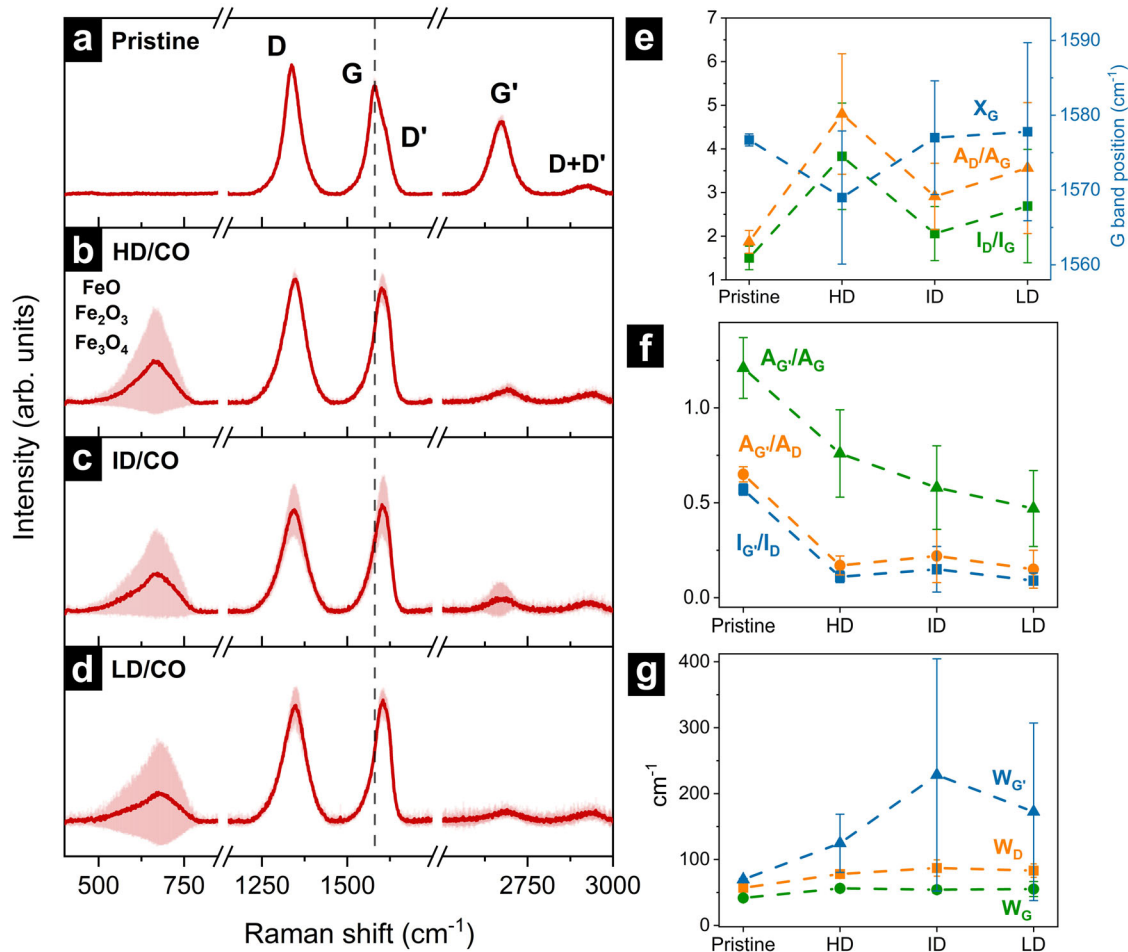


Fig. 5 Raman spectra and indicator developments of COs in pristine condition and after tribological testing. Raman spectra of **a** pristine COs and COs after tribological testing on **b** HD, **c** ID, and **d** LD surfaces, including standard deviation of spectral intensities (red area). Development of **e** I_{D}/I_{G} , A_{D}/A_{G} , X_{G} **f** $I_{G'}/I_{D}$, $A_{G'}/A_{D}$, $A_{G'}/A_{G}$ and **g** W_{D} , W_{G} , $W_{G'}$ with increasing structural depth (error bars represent standard deviation from three independent measurements).

likely to result from a more developed D'-band. Based on absolute indicator values, COs exhibit a stronger overall defectivity than CNTs. However, this type of comparison should be treated with caution as the curvature influences the Raman interaction of sp^2 -hybridized carbon (curvature-induced defect scattering)³⁹. COs are smaller than CNTs and three-dimensionally curved (0D carbon allotrope), implying a significantly stronger overall curvature. The results of this Raman analysis indicate that coated patterns with low structural depth lead to stronger degradation (along with superior lubricity, as shown in our previous work). This could be explained by the fact that low structural depths are generally associated with relatively flat slopes, which facilitate particle transfer from the depths of the grooves directly into the contact, where the particles are exposed to shear forces and, thus, deteriorate.

Electron microscopy characterization

Complementary to Raman analysis, cross-sectional transmission electron micrographs from the center of the wear tracks were prepared to study the nanocarbons' condition after friction testing.

On HD, the CNT-based tribofilm can be divided into three distinct areas representing different states of degradation (Fig. 6a). At the bottom of the groove, the CNTs remain in pristine condition with visible voids between the individual agglomerates (state 1). The area directly above can be identified as a transition zone

where the CNTs' porosity begins to fade due to increasing tribological loading and interaction with the tribological interface (state 2). The top layer was in direct contact with the counter body and, thus, directly exposed to shear stress, causing a full compression of the tribofilm (state 3). In addition, this layer incorporates and stores the resulting wear particles. Both films on ID and LD largely correspond to state 3, which is plausible considering the shallowness of the reservoirs (Fig. 6b, c). However, at the substrate/film interface on ID and LD, the shape of individual CNT agglomerates can be identified, indicating state 2.

A gradual decrease in overall crystallinity from HD to LD can be observed when comparing higher magnification TEM images of the tribofilms' near-surface zones (Pt-coating/film interface). On HD (Fig. 6d), large CNT fragments (contoured in teal) are present, whereas, on ID (Fig. 6e), the fragments are fewer and substantially smaller and contain noncrystalline domains (marked in red), which is not the case on HD. The tribofilm on LD (Fig. 6f) contains few, if any, and small crystalline domains. With a value of 3.48 Å, the interlayer spacing of the CNT fragments on HD lies above the literature range of 3.38–3.41 Å; (depending on chirality). It gradually increases further with decreasing depth, reaching 3.84 Å on LD. Generally, there is a tendency for the interlayer spacing to increase as deformation and/or degradation progresses⁴⁰.

The TEM images show that the CO-derived tribofilms (Fig. 7a–f) contain considerably more wear particles than their CNT-derived

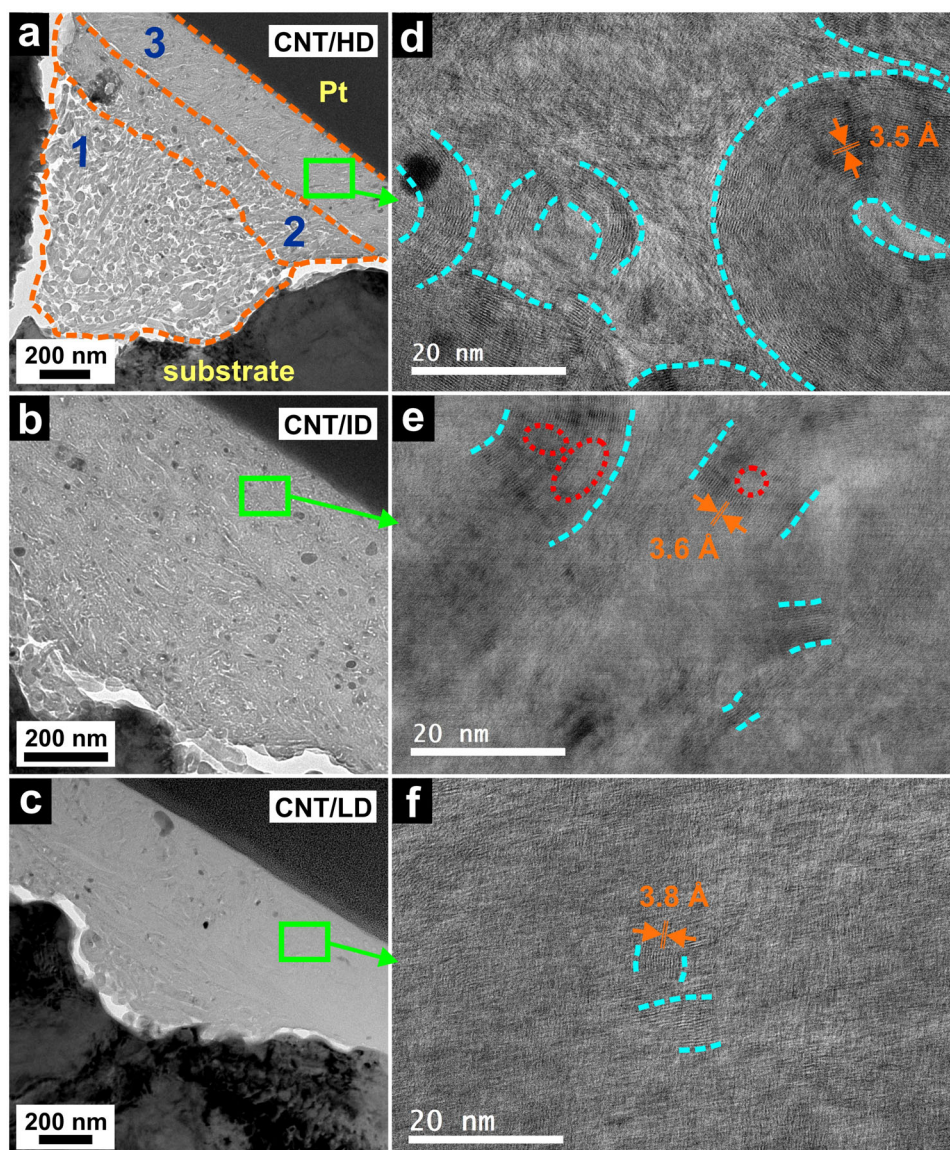


Fig. 6 Post friction test, cross-sectional TEM images of the CNT coatings. Representative images of the tribofilm at lower magnification on **a** HD, **b** ID, and **c** LD. Representative images of the tribofilm close to the interface at higher magnification on **d** HD, **e** ID, and **f** LD. Identifiable CNT fragments are contoured in teal. The red circles in (**e**) represent noncrystalline areas within the CNT fragments.

equivalents (Fig. 6a–f). Moreover, regardless of structural depth, none of the CO films show any signs of structural alteration at low magnification. However, transmission electron micrographs at higher magnification (Fig. 7d–f) show the tribofilms on HD (Fig. 7d) and LD (Fig. 7f) to contain few and small crystalline domains, similar to those on CNT/LD (Fig. 6f). The tribofilm on LD indicates stronger defectivity as the fragments are barely recognizable as such, whereas those on HD are larger. The spherical morphology of pristine COs^{5,41} appears to have vanished entirely at the tribofilms' topmost surface, likely due to heavy degradation causing the original particles to break down into smaller fragments that continue to degrade further until crystallinity disappears entirely. Exactly that seems to have occurred on ID (Fig. 7e), where no crystalline structures are detected. Simultaneously, the tribofilm on ID exhibits the highest wear particle concentration, which might have been a possible accelerator for particle degradation during tribological testing compared to LD and HD.

Raman and electron microscopy characterization of the CO- and CNT-derived tribofilms concurrently indicate strong overall deterioration due to tribological testing, with COs being

considerably more degraded. Several factors need to be considered to explain this outcome. In pristine conditions, COs are already more defective than the CNTs, as shown by Raman analysis. COs are also smaller and spherical (as opposed to cylindrical), which results in decreased mechanical (and chemical) stability as greater curvature is associated with stronger inherent strain⁴². In addition, contact pressures at the particle/counter body interface and between individual COs and/or agglomerates are increased during sliding as contact areas are smaller. It is also possible that some of the COs have remaining nanodiamond cores despite high-temperature annealing, which would cause additional inherent strain due to density differences between the graphitized shell and the sp^3 core⁴³. In conclusion, COs have an increased tendency to degrade under tribological stress compared to CNTs.

According to the Raman indicators, the COs on LD are the most defective, followed by HD and ID. In contrast, TEM analysis suggests ID is the most defective, followed by LD and HD. TEM images and Raman data, thus, do not match relative particle defectivity for COs, and a trend, as observed with the CNTs, is not

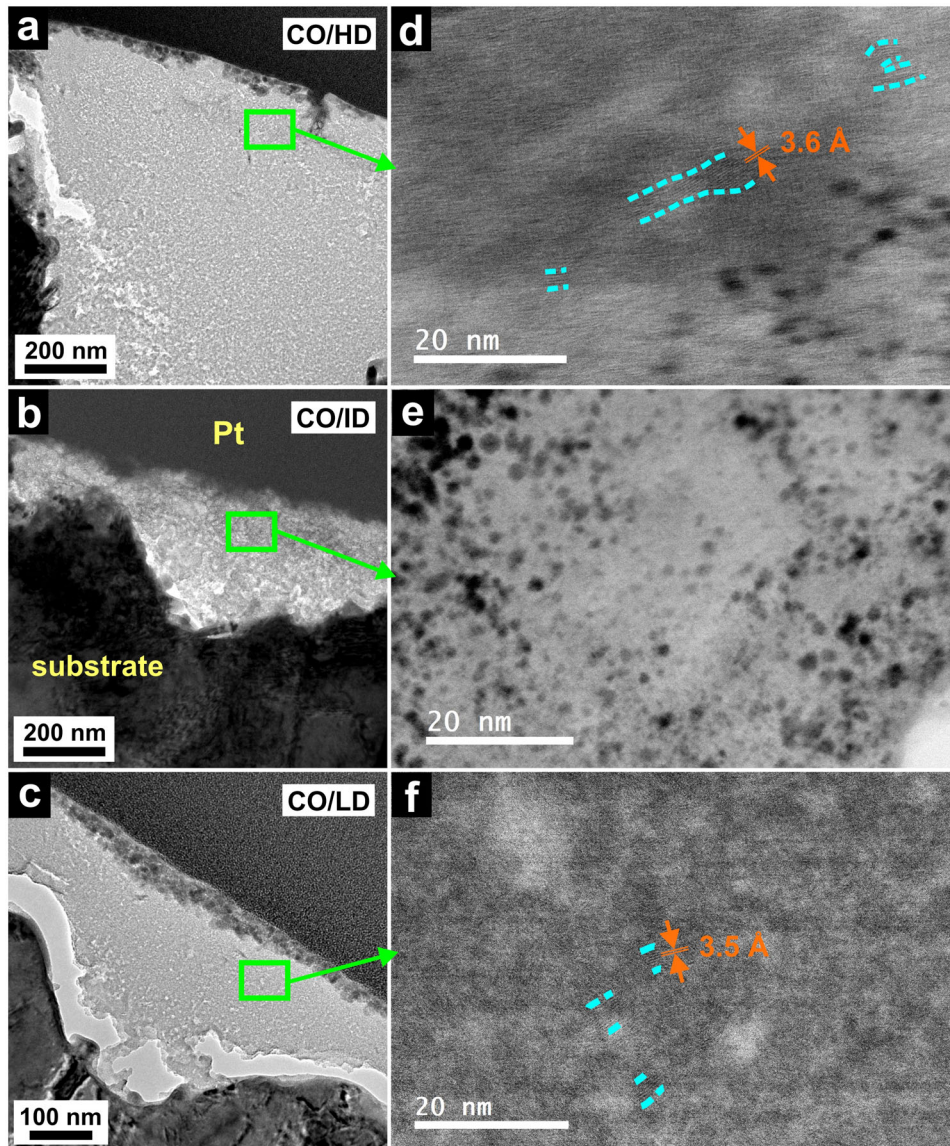


Fig. 7 Post friction test, cross-sectional TEM images of the CO coatings. Representative images of the tribofilm at lower magnification on **a** HD, **b** ID, and **c** LD. The gap between the substrate surface and tribofilm in (c) is a consequence of sample preparation. Representative images of the tribofilm close to the interface at higher magnification on **d** HD, **e** ID, and **f** LD. Identifiable crystalline fragments are contoured in teal.

discernible. However, directly comparing the results of both techniques is unsuitable due to the Raman signal's limited probing depth of the tribofilms; hence, both techniques should be viewed as complementary.

It was further shown that the COF of the CNTs (on all surfaces) and the COs on LD remain constant after running-in, although the particles become increasingly degraded. It has long been assumed that CNTs and COs behave similarly to a bearing in that they at least partially roll. Considering these results, rolling can be eliminated as the primary lubrication mechanism of CNTs and COs.

Summary of the results

This work provides an in-depth degradation analysis of CNT and CO coatings exposed to friction testing on laser-patterned AISI 304 stainless-steel surfaces with varying structural depths. The results demonstrate the occurrence of oxidation on all CO-coated wear tracks, regardless of structural depth, whereas none is detected in

any of the CNT-coated wear tracks. This finding agrees well with the EDS results of our previous work. Furthermore, obtained Raman indicator values of the CNTs are in good agreement with Reinert et al. despite differing testing parameters such as contact situation, load, and relative humidity²¹. Regarding particle classification within Ferrari's three-stage amorphization model, the CNTs are classified between pristine and nanocrystalline graphite, whereas the COs have entered the transition stage from nanocrystalline graphite to hydrogenated amorphous carbon, although no amorphous carbon was detected. These findings are consistent with TEM. Raman analysis further reveals a direct correlation between pattern depth, lubricity, and CNT degradation. More specifically, as CNT lubricity improves with shallowing patterns, the particles become more defective. TEM also confirms this as it shows gradually shrinking crystalline domains with decreasing structural depth. Characterization of the CO-derived tribofilm shows even more substantial structural degradation than observed with CNTs. This can be explained by the COs' spherical geometry combined with their smaller size, as both factors

contribute to stronger curvature and, thus, higher σ -bond tension. As a result, COs are less resistant to mechanical degradation. Finally, by demonstrating sustained and constant lubricity despite continuous particle degradation, rolling can be rejected as a lubrication mechanism of CNTs and COs.

METHODS

Material

Commercially available multiwall CNTs with an outer diameter of 30–85 μm , a length of 10–15 μm , and >98% purity were purchased at Graphene Supermarket. The COs used were synthesized by annealing detonation nanodiamonds (NaBond Technologies Co.) in a vacuum furnace (1100-3580-W1, Thermal Technology Inc.) at a temperature of 1700 $^{\circ}\text{C}$ for 1 h at a rate of 10 $^{\circ}\text{C min}^{-1}$ ^{43,44}. The resulting particle diameter is 4–8 nm, with a purity of >98%. After thoroughly cleaning with isopropanol and acetone, mirror-polished AISI 304 austenitic stainless-steel platelets (20 \times 20 mm^2 , Brio Kontrollspiegel GmbH) were used as substrate material.

Pulsed direct laser interference patterning

A neodymium-doped yttrium aluminum garnet (Nd:YAG) pulsed laser (Edgewave PX-series InnoSlab) integrated into a laser system RDX 500 nano (Pulsar Photonics) was used to create three different line patterns with structural depths of 0.22, 0.37, and 0.78 μm on the substrate surface with a periodicity of 3.5 μm at a pulse duration of 12 ps. The patterning process is described in greater detail elsewhere⁹.

Solution preparation and electrophoretic deposition

The deposition solution consisted of 80 ml of isopropanol, 10 ml of triethylamine (ACROS Organics, >99% purity), and 8 mg of carbon nanoparticle content. During the first step of dispersion, the solution was exposed to shear mixing using an Ultra-Turrax (T25 by IKA) for 10 min at 7000 rpm. The second step consisted of ultrasonication (Bandelin Sonorex RK514BH) for 10 min (CNT) and 45 min (CO). During the subsequent deposition, the patterned platelet and a nonpatterned but otherwise identical platelet used as a counter electrode were arranged in parallel and immersed in the solution. A DC voltage of 150 V was applied for the CNT-containing solution and 300 V for the CO-containing solution for 15 min.

Tribological testing

A ball-on-disc tribometer (CSM Instruments) was used in linear-reciprocating mode to investigate how the coefficient of friction (COF) evolves. Measurements were conducted at a normal load of 100 mN transversal to the line pattern at a stroke length of 0.6 mm and a velocity of 1 mm s^{-1} . Alumina balls (6 mm diameter, grade 28, Kugel Pompel HSI-Solutions GmbH) were chosen as a counter body. Further tribometrical specifications are described elsewhere⁹.

Electron microscopy

Scanning electron microscopy (SEM) images of the wear tracks were prepared using a Helios NanoLab 600 dual beam workstation equipped with a focused ion beam (FIB; FEI) at an acceleration voltage of 5 kV and a current of 1.4 nA. Transmission electron microscopy (TEM) at low magnification was conducted with a JEOL JEM 2010F at an acceleration voltage of 200 kV, whereas for high magnification TEM, a JEOL JEM-ARM200F was used at 200 kV. TEM foils were taken from the center of the wear track and prepared using the abovementioned Helios workstation.

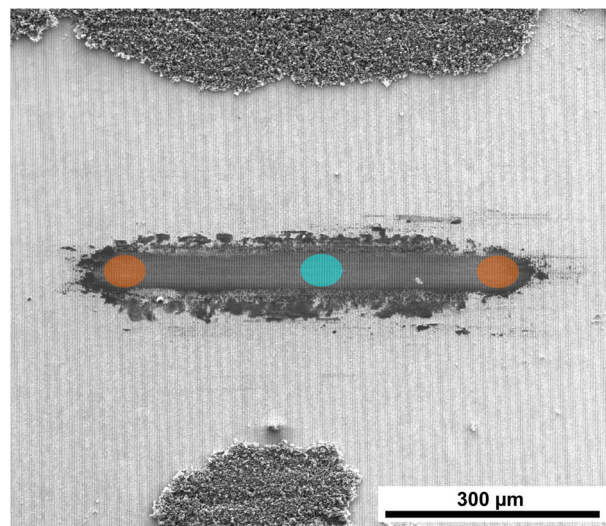


Fig. 8 Exemplary top view scanning electron micrograph of a CO-coated wear track (low depth laser pattern) post friction testing. This image marks the areas where the Raman measurements were conducted.

Raman spectroscopy

An inVia confocal Raman microscope (Renishaw) with a spectral resolution of 1.2 cm^{-1} was used to analyze the structural integrity of the remaining carbon nanoparticles in the resulting wear tracks after the tribological tests conducted in our previous work⁹. The spectra were acquired with an excitation wavelength of 532 nm, a laser power of 0.5% (corresponding to approximately 500 μW), a 50 \times -objective (numerical aperture: 0.9), and a grating of 2400 lines mm^{-1} . The spectrometer was calibrated using a single-crystal silicon sample. Measurements were conducted at three different spots in each wear track and outside (pristine). Inside the wear track, two measurements were taken in the center (Fig. 8, area marked in teal) and one at one of the edges (Fig. 8, area marked in orange). As for the pristine particles, measurements were taken on coating sections outside of the wear tracks. Automated processing of the gathered data included cosmic ray, background removal, and intensity normalization ([0,1]).

DATA AVAILABILITY

The data that support the findings of this study are available from the corresponding author upon reasonable request.

Received: 17 November 2022; Accepted: 20 March 2023;

Published online: 19 April 2023

REFERENCES

- Schäfer, C. et al. Influence of surface design on the solid lubricity of carbon nanotubes-coated steel surfaces. *Tribol. Lett.* **66**, 89 (2018).
- Reinert, L. et al. Long-lasting solid lubrication by CNT-coated patterned surfaces. *Sci. Rep.* **7**, 42873 (2017).
- MacLucas, T., Schütz, S., Suarez, S. & Mücklich, F. Surface protection of austenitic steels by carbon nanotube coatings. *Surf. Topogr. Metrol. Prop.* **6**, 14005 (2018).
- Reinert, L., Schütz, S., Suárez, S. & Mücklich, F. Influence of surface roughness on the lubrication effect of carbon nanoparticle-coated steel surfaces. *Tribol. Lett.* **66**, 45 (2018).
- Hirata, A., Igarashi, M. & Kaito, T. Study on solid lubricant properties of carbon onions produced by heat treatment of diamond clusters or particles. *Tribol. Int.* **37**, 899–905 (2004).
- Hirata, A. & Yoshioka, N. Sliding friction properties of carbon nanotube coatings deposited by microwave plasma chemical vapor deposition. *Tribol. Int.* **37**, 893–898 (2004).

7. Dickrell, P. L. et al. Tunable friction behavior of oriented carbon nanotube films. *Tribol. Lett.* **24**, 85–90 (2006).
8. Miyoshi, K., Street, K. W., Vander Wal, R. L., Andrews, R. & Sayir, A. Solid lubrication by multiwalled carbon nanotubes in air and in vacuum. *Tribol. Lett.* **19**, 191–201 (2005).
9. MacLucas, T. et al. Influence of structural depth of laser-patterned steel surfaces on the local lubricity of carbon nanoparticle coatings. *Friction* **11**, 1276–1291 (2022).
10. Chen, C. S., Chen, X. H., Xu, L. S., Yang, Z. & Li, W. H. Modification of multiwalled carbon nanotubes with fatty acid and their tribological properties as lubricant additive. *Carbon* **43**, 1660–1666 (2005).
11. Peng, Y., Hu, Y. & Wang, H. Tribological behaviors of surfactant-functionalized carbon nanotubes as lubricant additive in water. *Tribol. Lett.* **25**, 247–253 (2007).
12. Lu, H. F. et al. Synthesis and lubricating performance of a carbon nanotube seeded miniemulsion. *Carbon* **45**, 936–942 (2007).
13. Kristiansen, K., Zeng, H., Wang, P. & Israelachvili, J. N. Microtribology of aqueous carbon nanotube dispersions. *Adv. Funct. Mater.* **21**, 4555–4564 (2011).
14. Reinert, L., Suárez, S. & Rosenkranz, A. Tribo-mechanisms of carbon nanotubes: friction and wear behavior of CNT-reinforced nickel matrix composites and CNT-coated bulk nickel. *Lubricants* **4**, 11 (2016).
15. Reinert, L. et al. Tribological behavior of self-lubricating carbon nanoparticle reinforced metal matrix composites. *Wear* **408–409**, 72–85 (2018).
16. Scharf, T. W., Neira, A., Hwang, J. Y., Tiley, J. & Banerjee, R. Self-lubricating carbon nanotube reinforced nickel matrix composites. *J. Appl. Phys.* **106**, 013508 (2009).
17. Kim, K. T., Cha, S. I. L. & Hong, S. H. Hardness and wear resistance of carbon nanotube reinforced Cu matrix nanocomposites. *Mater. Sci. Eng. A* **448–451**, 46–50 (2007).
18. Suárez, S., Rosenkranz, A., Gachot, C. & Mücklich, F. Enhanced tribological properties of MWCNT/Ni bulk composites: influence of processing on friction and wear behaviour. *Carbon* **66**, 164–171 (2014).
19. Tan, J., Yu, T., Xu, B. & Yao, Q. Microstructure and wear resistance of nickel-carbon nanotube composite coating from brush plating technique. *Tribol. Lett.* **21**, 107–111 (2006).
20. Guiderdoni, C. et al. The preparation of double-walled carbon nanotube/Cu composites by spark plasma sintering, and their hardness and friction properties. *Carbon* **49**, 4535–4543 (2011).
21. Reinert, L., Varenberg, M., Mücklich, F. & Suárez, S. Dry friction and wear of self-lubricating carbon-nanotube-containing surfaces. *Wear* **406–407**, 33–42 (2018).
22. Dresselhaus, M. S., Dresselhaus, G., Saito, R. & Jorio, A. Raman spectroscopy of carbon nanotubes. *Phys. Rep.* **409**, 47–99 (2005).
23. Ferrari, A. & Robertson, J. Interpretation of Raman spectra of disordered and amorphous carbon. *Phys. Rev. B Condens. Matter Mater. Phys.* **61**, 14095–14107 (2000).
24. Cañado, L. G. et al. Quantifying defects in graphene via Raman spectroscopy at different excitation energies. *Nano Lett.* **11**, 3190–3196 (2011).
25. Ferrari, A. C. & Robertson, J. Resonant Raman spectroscopy of disordered, amorphous, and diamondlike carbon. *Phys. Rev. B Condens. Matter Mater. Phys.* **64**, 075414 (2001).
26. Brown, S. D. M., Dresselhaus, M. S., Jorio, A. & Dresselhaus, G. Observations of the D-band feature in the Raman spectra of carbon nanotubes. *Phys. Rev. B Condens. Matter Mater. Phys.* **64**, 073403 (2001).
27. Pimenta, M. A. et al. Studying disorder in graphite-based systems by Raman spectroscopy. *Phys. Chem. Chem. Phys.* **9**, 1276–1291 (2007).
28. Ferrari, A. C. & Basko, D. M. Raman spectroscopy as a versatile tool for studying the properties of graphene. *Nat. Nanotechnol.* **8**, 235–246 (2013).
29. Tuinstra, F. & Koenig, J. L. Raman spectrum of graphite. *J. Chem. Phys.* **53**, 1126–1130 (1970).
30. Martins Ferreira, E. H. et al. Evolution of the Raman spectra from single-, few-, and many-layer graphene with increasing disorder. *Phys. Rev. B Condens. Matter Mater. Phys.* **82**, 125429 (2010).
31. Lasagni, A. F. et al. Direct laser interference patterning, 20 years of development: from the basics to industrial applications. *SPIE Proc.* **10092**, 1009211 (2017).
32. Hiura, H., Ebbesen, T. W., Tanigaki, K. & Takahashi, H. Raman studies of carbon nanotubes. *Chem. Phys. Lett.* **202**, 509–512 (1993).
33. Thomsen, C. & Reich, S. Double resonant Raman scattering in graphite. *Phys. Rev. Lett.* **85**, 5214–5217 (2000).
34. Gontijo, R. N., Resende, G. C., Fantini, C. & Carvalho, B. R. Double resonance Raman scattering process in 2D materials. *J. Mater. Res.* **34**, 1976–1992 (2019).
35. Lehman, J. H., Terrones, M., Mansfield, E., Hurst, K. E. & Meunier, V. Evaluating the characteristics of multiwall carbon nanotubes. *Carbon* **49**, 2581–2602 (2011).
36. DiLeo, R. A., Landi, B. J. & Raffaele, R. P. Purity assessment of multiwalled carbon nanotubes by Raman spectroscopy. *J. Appl. Phys.* **101**, 064307 (2007).
37. Oh, S. J., Cook, D. C. & Townsend, H. E. Characterization of iron oxides commonly formed as corrosion products on steel. *Hyperfine Interact.* **112**, 59–66 (1998).
38. MacLucas, T., Leonhard-Trautmann, P., Suarez, S. & Mücklich, F. Long-term lubricity of carbon nanoparticle coatings on periodically laser-patterned metallic surfaces. *Tribol. Lett.* **70**, 123 (2022).
39. Podila, R., Rao, R., Tsuchikawa, R., Ishigami, M. & Rao, A. M. Raman spectroscopy of folded and scrolled graphene. *ACS Nano* **6**, 5784–5790 (2012).
40. Liu, M. & Cowley, J. M. Structures of carbon nanotubes studied by HRTEM and nanodiffraction. *Ultramicroscopy* **53**, 333–342 (1994).
41. He, C. N., Shi, C. S., Du, X. W., Li, J. J. & Zhao, N. Q. TEM investigation on the initial stage growth of carbon onions synthesized by CVD. *J. Alloy. Compd.* **452**, 258–262 (2008).
42. Haddon, R. C. Chemistry of the fullerenes: the manifestation of strain in a class of continuous aromatic molecules. *Science* **261**, 1545–1550 (1993).
43. Zeiger, M., Jäckel, N., Mochalin, V. & Presser, V. Review: carbon onions for electrochemical energy storage. *J. Mater. Chem. A* **4**, 3172–3196 (2015).
44. Zeiger, M., Jäckel, N., Aslan, M., Weingarh, D. & Presser, V. Understanding structure and porosity of nanodiamond-derived carbon onions. *Carbon* **84**, 584–598 (2015).

ACKNOWLEDGEMENTS

T.M. and S.S. wish to gratefully acknowledge financial support from the Deutsche Forschungsgemeinschaft (DFG, German Research Foundation) and Saarland University within the ‘Open Access Publication Funding’ program and project MU 959/47-1. Further funding by the ZuMat project, supported by the State of Saarland from the European Regional Development Fund (Europäischen Fonds für Regionale Entwicklung, EFRE), is kindly acknowledged. P.G. and C.G. would like to thank the Government of Lower Austria (WST3) for financially supporting the endowed professorship tribology at the TU Wien. The INM authors thank Eduard Arzt (INM) for his continuing support. Finally, the authors would like to express their gratitude to Prof. Marcos A. Pimenta (Federal University of Minas Gerais, BR) for his support with the Raman analysis.

AUTHOR CONTRIBUTIONS

T.M.: conceptualization, investigation, formal analysis, visualization, writing—original draft. P.G.: formal analysis, writing—review and editing. S.H.: formal analysis, writing—review and editing. J.S.: investigation. S.K.: methodology, S.S.: conceptualization, investigation, writing—review and editing. V.P.: resources, writing—review and editing. C.G.: supervision, formal analysis, writing—review and editing, funding acquisition. F.M.: supervision, resources, funding acquisition.

FUNDING

Open Access funding enabled and organized by Projekt DEAL.

COMPETING INTERESTS

The authors declare no competing interests.

ADDITIONAL INFORMATION

Correspondence and requests for materials should be addressed to T. MacLucas or C. Gachot.

Reprints and permission information is available at <http://www.nature.com/reprints>

Publisher's note Springer Nature remains neutral with regard to jurisdictional claims in published maps and institutional affiliations.



Open Access This article is licensed under a Creative Commons Attribution 4.0 International License, which permits use, sharing, adaptation, distribution and reproduction in any medium or format, as long as you give appropriate credit to the original author(s) and the source, provide a link to the Creative Commons license, and indicate if changes were made. The images or other third party material in this article are included in the article's Creative Commons license, unless indicated otherwise in a credit line to the material. If material is not included in the article's Creative Commons license and your intended use is not permitted by statutory regulation or exceeds the permitted use, you will need to obtain permission directly from the copyright holder. To view a copy of this license, visit <http://creativecommons.org/licenses/by/4.0/>.

© The Author(s) 2023